

SPIRAL Phase A: A Prototype Integral Field Spectrograph for the AAT.

Matthew A. Kenworthy¹ Ian R. Parry²

Institute of Astronomy, University of Cambridge, Madingley Road, Cambridge CB3 0HA

and

Keith Taylor³

Anglo Australian Observatory, Epping, Sydney, Australia

Received 4 April 2000; accepted 24 October 2000

Accepted by PASP

¹Electronic mail: mak@as.arizona.edu

²Electronic mail: irp@ast.cam.ac.uk

³Electronic mail: kt@astro.caltech.edu

ABSTRACT

We present details of a prototype fiber feed for use on the Anglo-Australian Telescope (AAT) that uses a dedicated fiber-fed medium/high resolution ($R \simeq 10000$) visible-band spectrograph to give integral field spectroscopy (IFS) of an extended object. A focal reducer couples light from the telescope to the close-packed lenslet array and fiber feed, allowing the spectrograph be used on other telescopes with the change of a single lens. By considering the properties of the fibers in the design of the spectrograph, an efficient design can be realised, and we present the first scientific results of a prototype spectrograph using a fiber feed with 37 spatial elements, namely the detection of Lithium confirming a brown dwarf candidate and IFS of the supernova remnant SN1987A.

Subject headings: instrumentation: spectrographs — stars: brown dwarfs, individual (LPP 944-20) — supernovae: individual (SN1987A)

1. INTRODUCTION

The Anglo-Australian Telescope (AAT) has pioneered many astronomical instruments over the past 25 years, such as the 2dF galaxy survey instrument (Taylor et al. 1997) and including one of the earliest reported fiber feeds in the literature (Gray et al. 1982). These instruments all use optical fibers to reformat the two dimensional distribution of light from the focal plane of the telescope into a one dimensional fiber slit suitable for a spectrograph, allowing multiple object (in the case of 2dF) and spatially resolved spectroscopy of extended objects.

Although there are many other methods used to perform integral field spectroscopy (IFS) the extremely versatile properties of optical fibers naturally lend themselves to optical reformatting (see Kenworthy 1998 for a review of IFS methods).

SPIRAL (Segmented Pupil/Image Reformatting Array of Lenslets) Phase A is an IFS design with 37 spatially resolved elements (see Figure 1) that has been built to prototype the new methods needed in building large integral field units (IFUs). Here we present a description and the first light results of SPIRAL Phase A.

EDITOR: PLACE FIGURE 1 HERE.

The design of SPIRAL considers the optical fibers as part of the spectrograph instead of an auxillary unit to a slit-based spectrograph.

In section 2 we analyse a simple fiber-fed spectrograph. The optical design can be simplified by optimising for dedicated fiber use. Section 3 then presents the design of the lens array, comparing the macrolens design with other methods of close packing fibers in the focal plane of the telescope. By using fore-optics to match the plate scale of the telescope with the lenslet array, the spectrograph can then be used with other telescopes by changing

a single lens.

The layout of SPIRAL Phase A is given in Section 4 along with the optical design for the fiber-fed spectrograph. Section 5 briefly covers the performance and accuracy of the fiber positioning technique that is used in the construction of the lens array and focal plane unit for SPIRAL Phase A. The performance of the spectrograph is given in Section 6 and preliminary scientific results are then presented in Section 7.

2. AN IDEALISED FIBER-FED SPECTROGRAPH

The internal transmission of an optical fiber is predominantly dependent on the wavelength of incident light and the focal ratio put onto the fiber. The material in the core of the fiber contributes absorption bands to the transmission properties beyond 700nm, predominantly from hydroxyl ions (see Schotz et al 1998). With recent low water content fibers, visible broad band transmission for lengths approaching many tens of meters and efficiencies of over 90% are available (Barden 1998).

Another dominant effect is focal ratio degradation (FRD), which has been characterised and analysed in great detail (see Barden 1988, Clayton 1989). Focal ratio degradation causes light entering a fiber at a given focal ratio to emerge into a larger cone-opening angle. FRD always acts to increase the etendue ($A\omega$ product) of light due to microbends and defects from an ideal cylindrical waveguide. The ideal focal ratio for most fibers is in the $f/3$ to $f/6$ range (Ramsey 1988).

By taking FRD into account, efficiencies nearing those for an uncoated fiber (92%) have been measured by constructing the receiving optics to accept a faster beam than is inputted into the fiber (Owen et al. 1998 and Rasilla et al. 1993). Properties of optical fibers are detailed in several reviews (e.g. Barden 1988; Barden 1998).

EDITOR: PLACE FIGURE 2 HERE.

To describe the IFS fiber setup, a single fiber fed with light from the telescope is shown in Figure 2. This can be broken down into two sections - a focal plane unit (FPU) that feeds light from the focal plane of the telescope into the fiber, and a spectrograph that disperses light from the fiber and images the spectrum onto the CCD camera. The angle of sky subtended by an individual fiber, α_{fiber} , is determined by the focal ratio of the light entering the fiber, f_{fiber} , the diameter of the fiber, D_{fiber} , and the diameter of the telescope, D_{tel} . α_{fiber} can therefore be written as

$$\alpha_{fiber} = \frac{D_{fiber}}{D_{tel} \cdot f_{fiber}}, \quad (1)$$

where D_{fiber} and D_{tel} are in the same units and α_{fiber} is in radians.

From conservation of etendue in optical systems (sometimes known as the $A \cdot \Omega$ product) this result can be extended throughout successive optics to give the angular extent of the fiber on the sky, regardless of the number of optics in front of it. From Equation 1 α_{fiber} is independent of the size of the optic used to feed it - it is only dependent on the focal ratio of the input beam.

The Anglo-Australian Telescope has a diameter of 3.9 metres, so for a fiber matched to 0.5 arcseconds on the sky and a core diameter of $50\mu\text{m}$, this requires an input focal ratio of $f/5.0$, which is a good compromise between spectrograph cost (faster optics are more expensive) and fiber efficiency (FRD is more detrimental to throughput at slower focal ratios).

Optics in the FPU re-image the star or telescope pupil onto the end of the fiber with a focal ratio of f_{fiber} . The input focal ratio of the spectrograph (which is identical to the focal ratio of the collimator, f_{coll}) should equal the focal ratio of the light entering

the fiber, i.e. $f_{coll} = f_{fiber}$, representing an ideal fiber with no FRD. This is the case for slit-based spectrographs, where the slit replaces an ideal fiber. For fiber-fed spectrographs the collimator is made slightly faster to accommodate the intrinsic FRD of the fiber ($f_{coll} < f_{fiber}$).

From the collimator of the spectrograph, the light then passes through the dispersing element and camera with focal ratio f_{camera} to form a fiber spectrum. The diameter of the image of the fiber on the detector is:

$$d_{image} = \frac{D_{fiber} \cdot f_{camera}}{f_{coll}}, \quad (2)$$

where D_{fiber} is the diameter of the core of the fiber in microns, and d_{image} is the diameter of the fiber image in microns.

The simplest FPU is one with no re-imaging optics and f_{fiber} is equal to the focal ratio of the telescope, f_{tel} . This design is used in many multi-object spectrographs where fibers have to be packed closely together on the focal plane of the telescope in order to sample crowded science fields, such as 2dF (Taylor et al. 1997), Autofib-2 (Bridges 1998) and FLAIR (Parker et al. 1998). This is not an ideal coupling of the telescope to the optimal fiber focal ratio, and for other applications fore-optics in the form of one or two lenses are introduced between the focal plane of the telescope and the fiber ends to change the focal ratio input put into the fibers.

Many of the first fiber-feeds were built as an add-on to existing slit-based spectrographs, resulting efficiencies much lower than expected. By designing the spectrograph around the properties of the optical fibers, a more efficient spectrograph could be built that exploits their versatile image reformatting capabilities.

3. LENSLET ARRAYS

Covering the focal plane of the telescope with a close packed array of lenslets allows bi-dimensional spectroscopy of an extended region of the sky. These lenslets tessellate to form a continuous pattern, with the fibers reformatting the light from the lenslets into a fiber slit to be fed into the spectrograph.

In order to optimally sample the spatial structure of an astronomical object, the plate scale of the lenses is such that the angular diameter of the fiber is half the FWHM diameter of the telescope point spread function. Given that the seeing disk diameter on most telescopes is typically 0.5 arcseconds and the plate scale of most large telescopes is on the order of hundreds of microns per arcsecond, the expected lenslet diameter is typically $350\mu\text{m}$. This situation worsens in large adaptive optic telescope systems where the lenslet size tends to smaller image scales. In the cases where a direct match to the plate scale of the telescope is needed, a microlens array is used (see Figure 3).

EDITOR: PLACE FIGURE 3 HERE.

Microlens arrays have a lenslet pitch of typically $150 - 500\mu\text{m}$ and differ from macrolens arrays (see below) in that their lenslet surfaces are manufactured in bulk on an optical substrate. One method involves the use of a metal template repeatedly stamped into a suitable substrate, whilst another method uses the controlled curing of epoxy resin on a suitable optical flat to form the lenslet surface. These give rise to square or hexagonal close packed arrays that have a highly regular spacing between lenslets, but the manufacturing process makes them prone to large levels ($\sim 10\%$) of scattered light (Lee et al. 1998).

Alignment of the fibers with the microlens array is done by use of a regular array of steel ferrules that match the lenslet pitch. Fibers are fixed into the steel ferrule array and

after optical polishing the fibers in the ferrule array are registered with the lenslet array. This method has been adopted by many groups, especially where IFS is being considered as an add-on to an existing spectrograph and the microlens array needs to match the existing plate scale of the telescope, such as the SMIRFS-IFS for the CGS4 spectrograph (Haynes et al. 1999).

From Equation 1 the angular extent of the fiber on the sky is dependent on its input focal ratio but independent of the size of lenslets used in the FPU. Thus the lenslet array pitch is not constrained and a macrolens array with a focal reducer can be used in place of a microlens array. This technique was first suggested in the early 1980's (Courtes 1982), pioneered in Russia on the SAO 6-meter telescope (Afanasiev et al. 1990) and is the one we use in SPIRAL Phase A.

Macrolens arrays are lenslet arrays manufactured from individual glass singlet or doublet lenses, with typical array pitches of 1mm - 5mm. These lenslets are cemented onto an achromatic flat whose optical thickness is equal to the focal length of the lenslets. Each fiber is then individually aligned with its respective lenslet, as opposed to microlens arrays where optical alignment is dependent on the pitch accuracy of the steel ferrule array holding the fibers. Macrolens arrays have the potential for lower scattered light losses and by using achromatic doublets greater wavelength coverage in the visible and near infra-red can be gained. The relative merits of macro- and microlens arrays are discussed further in other papers (Parry et al. 1997).

4. OPTICAL LAYOUT OF SPIRAL PHASE A

EDITOR: PLACE FIGURE 4 HERE.

Figure 4 shows the layout of the spectrograph on the telescope. A tilted aluminium

mirror sits in the focal plane of the telescope. A hole in the middle of the mirror allows light from the object to pass through to the fore optics whilst the surrounding field of view is imaged off the telescope axis by the target acquisition camera. Light passes through to the fore optics and into the lens array. All of these optical components are fixed onto an optical table in the Cassegrain cage. Optical fibers connected to the back of the lens array pass through the first strain relief box and out of the cage, down to the spectrograph sitting on the floor of the observatory. A second strain relief box on the outside of the spectrograph leads to a fiber slit where the fibers are reconfigured into a suitable straight slit. The light is dispersed in the spectrograph and the fiber spectra imaged on a CCD mounted inside a liquid nitrogen cooled vacuum dewar.

4.1. Fore-optics and Lenslet Array

EDITOR: PLACE FIGURE 5 HERE.

37 singlet lenses (PSK53A glass) spatially sample the sky in a close packed hexagonal pattern. Each lenslet is 4 mm across opposite corners and the array measures 20 mm in diameter. Optimum sampling occurs when two spatial elements match the typical seeing of the telescope (Nyquist sampling) and with a median seeing of one arcsecond. On the AAT this corresponds to a scale of 0.5 arcseconds per lenslet, giving a hexagonal array of 3.5 arcseconds across the corners.

Light from the telescope focus passes into a magnifying lens FOL1 which produces an image of the telescope pupil (the primary mirror). The field lens in front of the array images all the fiber faces in the IFU onto this common pupil (see Figure 5). Each lenslet then takes the section of sky image and projects an image of the pupil onto the end of the fiber behind it.

The lenslet array is mounted on an achromatic flat composed of 4.46 mm of SF6 flint glass and 29.77 mm of PSK53A Crown glass. The effective focal ratio of the lenslets on the flat is $f/5.0$. 37 lenslets were selected from a batch of 50, selected on the basis of surface quality and focal length.

The image of the AAT telescope pupil completely fills the $50\mu\text{m}$ core of the fiber. However, by adjusting the power of the magnifying lens FOL1, the sampling on the sky can be changed. By making the image scale less than 0.5 arcseconds per lenslet, the image of the telescope pupil becomes smaller and under-fills the fibers. This allows smaller scales to be observed without loss of efficiency. In SPIRAL Phase A the scale is set to 0.5" per lenslet giving a total field of view of 3.5 arcseconds.

EDITOR: PLACE FIGURE 6 HERE.

The fibers in the fiber slit correspond to lenslets in the array in a pre-defined pattern, so that images of the sky can be reconstructed from reduced fiber spectra (see Figure 6). The fiber slit is constructed so that fibers in the slit come from adjacent areas on the sky. Any cross-talk introduced by the extraction of overlapping fiber spectra are subsequently from adjacent areas in the observed field, preventing spurious introduction of artefacts in the reconstructed integral field image.

In extreme cases of cross-talk this results in an elongation of extended objects in the reconstruction. Since the SPIRAL spectrograph is designed to be used with 500 fibers in the Phase B fiber feed, the 37 fibers in the prototype were widely spaced apart along the length of the imaging area of the spectrograph slit and there was no cross-talk.

4.2. The Fiber Feed

The SPIRAL fibers were from Polymicro and made from fused silica. The core diameter was $50\mu\text{m}$, with a lower-index doped fused silica cladding out to $70\mu\text{m}$ diameter and a polyamide coating up to $90\mu\text{m}$. A further environmentally protective layer of soft polyethylene prevented damage of the fiber during handling, but was easily removed by soaking in acetone prior to fixture in the instrument.

A slow curing two-component epoxy mechanically holds the fiber within a thin stainless steel tube. Successively larger steel tubes were added and fixed in place to form a composite stainless steel tube with an outer diameter of $500\mu\text{m}$ and a single fiber held rigidly in the center.

The 37 fibers then pass into a protective polyamide tubing which guides the fibers with minimum bending into a tough, steel wound plastic covered conduit. This conduit passes through the Cassegrain cage of the telescope and down to the floor of the observatory. One meter from each end of the conduit is a strain relief box, where the fiber passes in an unsupported loop across the inside of the box before passing through out the other side. These two spare length boxes ensure that the expansion and contraction of the flexible conduit does not stretch and break the inelastic and delicate optical fibers.

The fiber passes into the fiber slit assembly. Here the 37 fibers are rearranged into a straight line, the fibers spaced evenly along the slit and parallel to each other. The fibers are held against a flat reference plate by a metal block with accurately machined grooves in its surface. The mechanical pressing action of the grooves and reference plate serve as a vice with which to hold the fibers in place. All fibers lie parallel to each other in a plane perpendicular to the surface of the final fiber slit. Epoxy resin is used to fill the inter-fiber spacing and provide a strong mechanical support for the fibers in the slit block. Finally a thin cover slit was fixed with optical cement across all the ends of the fibers in the polished

fiber slit. In this way, any scratches and imperfections in the ends of the fibers were filled in with index-matching cement and the exposed surface of the cover slip was coated with an anti-reflective layer of magnesium flouride.

Our fiber feed design has no exposed optical fiber surfaces, an important consideration when the active optical surface is $50\mu\text{m}$ in diameter. Left unprotected, the smallest scratch or contamination with dust can lead to a significant loss of efficiency. Both ends of the fiber feed are mated against a glass surface with a liquid optical cement, making an index matching interface and reducing scattering and reflection losses. The addition of a magnesium flouride anti-reflection coating to both ends of the fiber feed optics further improves the throughput.

4.3. The Spectrograph

The input focal ratio for the spectrograph is $f/4.8$, slightly faster than the $f/5.0$ beam entering the fibers. This allowed for FRD broadening of the beam. The spectrograph also had to produce monochromatic images over the whole area of the Tek CCD, requiring imaging of a slit length of 25 mm.

The SPIRAL spectrograph was designed by Damien Jones to use the Tek 1024×1024 pixel optical CCD. The $24\mu\text{m}$ pixels of this CCD give Nyquist sampling of the $50\mu\text{m}$ fiber diameter, which defines the entrance slit width to the spectrograph. Because this fixed slit width is smaller than most slit based spectrographs and is independent of the slit-adjusted seeing, the camera and collimator are combined to make a double pass system with a total magnification of unity. This then allows the grating to be used in a near-Littrow configuration with the grating used at its highest theoretical efficiency. For a double pass system the Littrow condition is exact only for object and image superimposed on each

other, but by separating the fiber slit and detector beams by 22.5 mm, the deviation from the Littrow configuration is minimised.

EDITOR: PLACE FIGURE 7 HERE.

The resultant design is shown in Figure 7. The most suitable optical configuration for the spectrograph is a field-flattened Petzval system, otherwise known as a P1 Petzval configuration. This consists of two separated positive doublets (L2 and L3) followed by a field flattening singlet (L1) near the focal plane. A small reflex prism brings the fiber slit image close to the optical axis of the system, and the grating G1 sits in the collimated space beyond L3.

The design also allows for rotation and tilt of the dewar, eliminating the need for an extra field correcting lens and thus reducing the cost of the system - a plot of chromatic focal shift (Figure 8) shows the extent of refocusing needed across the wavelength range of the spectrograph.

EDITOR: PLACE FIGURE 8 HERE.

5. FIBER POSITIONING

5.1. Mechanical Alignment of Fibers with Individual Lenslets

The macrolens array allowed individual positioning of fibers on the back of the lenslet array. Individual $50\mu\text{m}$ diameter fibers were fixed with epoxy resin into metal ferrules 10 mm long and with an outer diameter of $230\mu\text{m}$. Further steel ferrules were added to the outer diameter of this ferrule to produce a composite ferrule fiber holder 2 mm in diameter

with the optical fiber held firmly along the ferrule axis. All the fibers for the lens array were prepared this way and then placed together in a polishing jig. This jig was then used to simultaneously polish all 37 fiber faces and ferrules to optical quality.

The field lens FOL2 from the fore-optics was fixed in front of the lenslet array and a graticule was placed in the focal plane of the field lens with the cross-hairs centered on the optical axis of the field lens (see Figure 9). An electronic camera with a narrow-band filter and a microscope objective was focused on the cross-hair graticule. In a perfectly constructed IFU, the field lens brings all the individual fiber images from the lenslet array and brings them to a common focus on the center of the graticule. By back illuminating each fiber and using an x,y,z stage to manoeuvre the fiber ferrule, each fiber could be individually aligned with the optical axis of its respective lenslet.

EDITOR: PLACE FIGURE 9 HERE.

When the fiber image was centered in the graticule, the fiber was correctly aligned. The optical cement was applied to the face of the fiber to fix it to the back of the lens array, and any dust or air bubbles that existed between the fiber and lenslet array could be clearly seen in an electronic camera image and removed. When the fiber was ready, a UV source was used to cure the cement and fix the fiber in place.

After all 37 fibers were positioned, the lenslet array was assembled into an aluminium protective housing and a slow curing potting compound was poured onto the back of the lens array and in between the fiber ferrules. This increased the mechanical support of the ferrules and prevented sudden mechanical shocks from breaking the UV cement bond between ferrule face and lenslet array.

5.2. Measured Positioning Errors

In the fore-optics, lens FOL1 forms a pupil image of the telescope. This pupil is then re-imaged with FOL2, through each individual lenslet and forms a pupil image on the fiber face. If light is shone back up the fibers to illuminate all the lenslets, an image of each fiber is formed at the position of the telescope pupil - if all the fibers are concentric with the optical axis of their respective lenslet and all 37 fiber face images overlap exactly at the focus of FOL2.

If the fibers are not perfectly aligned then the fiber images do not overlap exactly, and each fiber image has a measured displacement from the mean position of all the combined images. From the image scale of the fiber image, the positional error in the fiber plane can be calculated.

We define the decentering error to be the radial distance of one fiber from the mean fiber position of the whole fiber feed. Assuming the positioning errors to be random and independent of each other, all the decentering errors form a Gaussian distribution around a mean fiber position and we can define an RMS decentering error for all the fibers that gives a measure of all the fiber misalignments in the lenslet array.

After the SPIRAL IFU was assembled, a measurement of the fiber positions was made using the alignment apparatus and the graticule cross hairs. The RMS decentering error was $10\mu\text{m}$ with a maximum error of $13\mu\text{m}$ (see Figure 10). This value was considerably larger than expected, and disagreed strongly with the value estimated by eye during the assembly of the lenslet array.

The reason for this large error was that the potting compound had displaced the fiber ferrules and caused a misalignment of the ferrules as it cured. Further investigation revealed that the optical cement used to hold the fibers in place on the lenslet array

required considerably longer exposure to the UV source than had been suggested in earlier experiments. This resulted in the fibers not being held firmly on the back of the lens array, and subsequently led to a calculated reduction of transmission efficiency of 20% in the fiber feed due to misalignment of the fibers and lenslets.

EDITOR: PLACE FIGURE 10 HERE.

The lenslet array could not be rebuilt without causing considerable damage to the fibers, so we used the prototype in its current state. The alignment technique was more accurate than the SPIRAL lenslet array, and the same method was used in the construction of a 100 element infra-red IFU for the Cambridge OH Suppression Instrument (COHSI) (Ennico 1998).

The technique was vindicated when the constructed lenslet array of 100 lenslets was measured to have an RMS decentering error of $3\mu\text{m}$ (Kenworthy et al. 1998b).

6. PERFORMANCE OF THE FIBER FEED AND SPECTROGRAPH

EDITOR: PLACE FIGURE 11 HERE.

Figure 11 shows a data frame taken with the SPIRAL Phase A spectrograph. An overscan and zero level frame has been subtracted, and cropped to remove stray and reflected light from the edge of the image. This exposure clearly shows absorption bands in the twilight sky.

6.1. Point Spread Function

The point spread function across the CCD was measured by fitting Gaussian profiles to an arc lamp frame containing many narrow emission lines. These proved ideal for measuring the PSF introduced by the spectrograph optics.

The PSF was measured to be 2.31 ± 0.11 pixels, corresponding to an image size of $69.3 \pm 0.3 \mu\text{m}$, larger than the fiber core diameter of $50 \mu\text{m}$, but in agreement with the PSF of the optical model as produced with commercial ray tracing software. There was no significant variation in the measured PSF across the image.

6.2. Spectral Range and Resolution

Different gratings were inserted into the spectrograph and arc spectra images were taken for various wavelength ranges. By using a dome flat field to define the fiber tracks the spectra were extracted and a dispersion solution identified for the arc lines. The best low-order fit for the dispersion was a 4th order polynomial. The results for three configurations are shown in Table 1.

EDITOR: PLACE TABLE 1 HERE.

6.3. Total Transmission

Observations of spectrophotometric standard stars provided an estimate of the throughput of the spectrograph and fiber feed. A two-dimensional low-order polynomial was fitted to a standard star data frame to remove scattered light. The frame was then summed along the dispersion axis to form a one-dimensional spectrum which was dispersion

corrected and wavelength calibrated.

Over three nights the SPIRAL spectrograph was calculated to have an efficiency of between 10-15% with an estimated median value of 12% at 6250\AA . The main variation in throughput was due to the fiber misalignment discussed in Section 5.2. By estimating and measuring the throughput of all the optical components in the system, the throughput of the IFU and fiber feed throughput was estimated to be $57 \pm 3\%$ (see Table 2). The throughput of the fore-optics, IFU and fiber feed combined is $52 \pm 3\%$, but if there was no fiber misalignment then this number increases to $65 \pm 3\%$.

EDITOR: PLACE TABLE 2 HERE.

7. FIRST RESULTS FROM SPIRAL A

At the beginning of our observing the MIT/Lincoln Laboratory 2048×4096 pixel CCD became available for use in the spectrograph. With its higher quantum efficiency and lower readout noise, we used this for the observations. Since this CCD has $15\mu\text{m}$ square pixels the MIT/LL was set to 2 by 2 pixel binning, forming a effective frame of 1024×2048 $30\mu\text{m}$ pixels.

7.1. Supernova 1987A

To test the integral field mode of SPIRAL, an object with small scale detail was required for our 3.5 arcsecond field. The Large Magellanic Cloud SN 1987A was observed during sub-arcsecond seeing on 1997 November 23.

EDITOR: PLACE FIGURE 12 HERE.

The circumstellar environment of the supernova is still not well understood (Crotts 1997). An HST optical image with the SPIRAL field of view is shown in Figure 12. The three ring structure which is visible in the image lies on the surface of an hourglass shape inclined partially to our line of sight (Crotts et al. 1989). The inner ring marks the waist of the hourglass (Crotts and Heathcote 1991) whilst the two larger rings mark a circumference further up the lobes, delineating the extent of a double-lobe nebula (Crotts et al. 1995).

The observations consisted of two sets of data frames. Three 1800 second exposures were taken of the supernova along with three 1200 second exposures of the adjacent sky. This was especially important as the supernova is within an HII region, with the associated nebular emission from various lines such as [O III] and [N II].

Figure 13 shows [O I] λ 6300, [N II] λ 6548, H α λ 6563, [N II] λ 6583, [S II] λ 6716 and [S II] λ 6731 emission lines. The supernova spectra have been background subtracted. However, some sky emission lines still remain from incorrect background subtraction.

EDITOR: PLACE FIGURE 13 HERE.

Nebular emission lines in the LMC are red shifted by its recession velocity (typically 300 km s^{-1}) and are visible in the spectra. The bright narrow H α line is predominantly from the supernova and this line is mapped in Figure 14. A lower intensity profile broadening of $\sim 2600 \text{ km s}^{-1}$ is visible in the spectrum. This is identified as the first signs of the fast moving supernova ejecta hitting and shocking slow moving circumstellar gas released during the progenitors giant star phase (Chevalier 1992 and Sonneborn et al. 1997).

Four maps have been generated which show the structure in the region of the supernova (Figure 14). The bulk of the continuum emission is from Star 2, in the South-east of the field of view. Selecting a similiar bandpass to the HST filter shows similiar intensity structure, and by fitting profiles to the supernova wind, the location of the supernova is

confirmed. An [N II] map shows an inner ring that has been shock-ionised by the initial UV flash from the explosion.

EDITOR: PLACE FIGURE 14 HERE.

7.2. Detection of a Brown Dwarf

To test the high resolution capability of the spectrograph several brown dwarf candidates were examined. One of the simplest tests for young brown dwarfs is detection of the Lithium absorption line Li I λ 6707.8 in very red objects with low absolute magnitude. This implies that the core temperature of the star has not reached the Li/H burning temperature and therefore not reached a higher H/H burning temperature (Rebolo et al. 1992). A more detailed discussion about the selection procedure can be found in (Kenworthy 1998).

EDITOR: PLACE FIGURE 15 HERE.

A list of candidate stars was provided by Hugh Jones (private communication) and the first star observed was LP 944-20. The observation was 1800 seconds with the 1200R grating used in second order, providing a calculated spectral resolution of 15000. As of mid-1997, when these observations were undertaken, there were only a small number of known brown dwarfs. LP 944-20 showed strong Li I absorption (see Figure 15) thus confirming its membership to this select group. However, during our observations a spectra from the CASPEC echelle spectrograph and ESO telescope was published (Tinney 1998) showing Li I absorption.

This now provided an excellent opportunity to compare the accuracy of the SPIRAL spectrograph with a standard slit-based spectrograph (see Table 3).

EDITOR: PLACE TABLE 3 HERE.

Both methods to determine the apparent magnitude and Lithium absorption agree within errors, with the only disagreement being the heliocentric velocity. Tinney derived the velocity by cross-correlation with a standard star, whilst the SPIRAL estimate was made with the centroid of the Lithium line only, resulting in the larger error estimate of the SPIRAL spectrograph.

8. SUMMARY

We have manufactured a lenslet array from individual lenslets and demonstrated that fibers can be aligned with these lenslets to $3\mu\text{m}$ RMS error, providing an alternative technique to the microlens array method. The use of fore-optics makes the fiber feed portable and the use of fibers leads to a simplified and more efficient spectrograph design.

Integral field observations of a supernova remnant allow maps of spatial variations in spectral line properties to be generated, and high spectral resolutions to be achieved. The success of this prototype led to the construction of SPIRAL Phase B and its commissioning in May 2000.

We are indebted to the Staff and Technicians of the Anglo-Australian Observatory, who were always ready to help out in getting the instrument on the telescope. MAK thanks Karl Glazebrook and Dave Lee, who provided invaluable help with the software and calibration on the observing runs, and to Richard Ogley for proof-reading this paper.

REFERENCES

- Afanasiev, V.L., Vlasiuk, V.V., Dodonov, S.N., Sil'chenko O.K. 1990, SAO Preprint No. 54
- Barden, S.C. 1988, in ASP Conf. Ser. 3, Fiber Optics in Astronomy I, ed. S.C. Barden, Section 1
- Barden 1998, in ASP Conf. Ser. 152, Fiber Optics in Astronomy III, ed. S. Arribas, E. Mediavilla, F. Watson, 14
- Bridges, T. 1998 in ASP Conf. Ser. 152, Fiber Optics in Astronomy III, ed. S. Arribas, E. Mediavilla, F. Watson, 104
- Chevalier R. 1992, ApJ 258, 790
- Clayton, C.A. 1989, A&A 213, 502
- Courtes, G. 1982, in Instrumentation for Astronomy with Large Optical Telescopes, ed. C.M. Humphries, 123
- Crotts, A.P.S., Kunkel, W.E., McCarthy, P.J. 1989, ApJ 347, L61
- Crotts, A.P.S., Kunkel, W.E., Heathcote S.R. 1995, ApJ 438, 724
- Crotts, A.P.S., Heathcote S.R. 1991, Nature 350, 683
- Crotts, A.P.S. 1997 in SN 1987A: Ten Years After, ed. M. Phillips, N. Suntzeff, 28
- Ennico, K. 1998, Ph.D. thesis, Univ. Cambridge
- Gray, P.M., Phillips, M.M., Turtle, A.J., Ellis, R. 1982, Proc. ASA 4(4)
- Haynes, R., et al. 1999, PASP 111, 1451
- Kenworthy, M.A. 1998, Ph.D. thesis, Univ. Cambridge

- Kenworthy, M.A., Parry I.R., Ennico, K.A. 1998 in ASP Conf. Ser. 152, Fiber Optics in Astronomy III, ed. S. Arribas, E. Mediavilla, F. Watson, 300
- Kirkpatrick, J.D., Henry, T.J., Irwin, M.J. 1997, AJ 113, 1421
- Lee, D., Allington-Smith, J., R. Content, R., Haynes, R., Proc. SPIE 3355, 810
- Owen, R.E., Buffaloe, J., French Leger, R., Mannery, E.J., Siegmund, W.A., Waddell, P., Hull, C.L. 1998 in ASP Conf. Ser. 152, Fiber Optics in Astronomy III, ed. S. Arribas, E. Mediavilla, F. Watson, 98
- Parker, Q.A., Watson, F.G., Miziaski, S. 1998 in ASP Conf. Ser. 152, Fiber Optics in Astronomy III, ed. S. Arribas, E. Mediavilla, F. Watson, 80
- Parry, I.R., Kenworthy, M.A., Taylor, K. 1997, Proc. SPIE 2871, 1325
- Ramsey, L.W. 1988, in ASP Conf. Ser. 3, Fiber Optics in Astronomy I, ed. S.C. Barden, 26
- Rasilla, J.L., Garcia Marin, A., Arribas, S. 1993 Ser. 152, Fiber Optics in Astronomy II, ed. P.M. Gray, 203
- Reboloi, R., Martin, E.L., Magazzu, A. 1992, ApJ 389, 93
- Schotz, G.F., Vydra, J., Lu, G., Fabricant, D. 1998 in ASP Conf. Ser. 152, Fiber Optics in Astronomy III, ed. S. Arribas, E. Mediavilla, F. Watson, 20
- Sonneborn, G., et al. 1997, ApJ 492, 139
- Taylor, K., Cannon, R.D., Watson, F.G. 1997, Proc. SPIE 2871, ed. A.L. Ardeberg, 145
- Tinney, C.G. 1998, MNRAS 296, L42

Table 1. Measured dispersions and resolutions of the SPIRAL spectrograph

Grating	Wavelength Range (Å)	Dispersion (Å/pixel)	Line FWHM (Å)	Spectral Resolution (R)
270R 1st order	2400	1.525	2.820 ± 0.180	2730
1200R 1st order	500	0.314	0.864 ± 0.036	7550
1200R 2nd order	250	0.155	0.419 ± 0.017	15000

Table 2. Measured and estimated efficiencies for SPIRAL Phase A on the AAT

Optical Component	Transmission (% at 6000Å)
Atmosphere and telescope	56 ± 1^a
Fore-optics	92 ± 1^b
IFU and fiber feed	57 ± 3
Spectrograph and 1200R grating	53 ± 1^c
CCD	77 ± 1^c
Total measured efficiency	12 ± 2

^aKarl Glazebrook (priv. commun.)

^bEstimated for 4 air-glass surfaces

^cDave Lee (priv. commun.)

Table 3. Comparison of measured properties of LP 944-20

	Apparent Magnitude (m_R)	EW of Li I (\AA)	Heliocentric Velocity (km s^{-1})
Value from literature	$17.1 \pm 0.1^{\text{a}}$	0.53 ± 0.05	$+13 \pm 4^{\text{b}}$
Value from SPIRAL A	17.19 ± 0.10	0.54 ± 0.06	-22 ± 12

^aKirkpatrick et al. 1997

^bCross-correlation with reference star

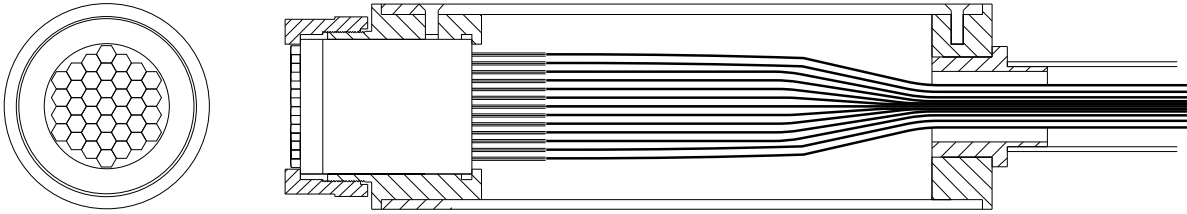


Fig. 1.— The SPIRAL Phase A Integral Field Unit. The front view (left) shows the arrangement of the 37 hexagonal lenslets and the cutaway side view (right) shows the metal casing and fiber optics from the lenslets leading down to the spectrograph.

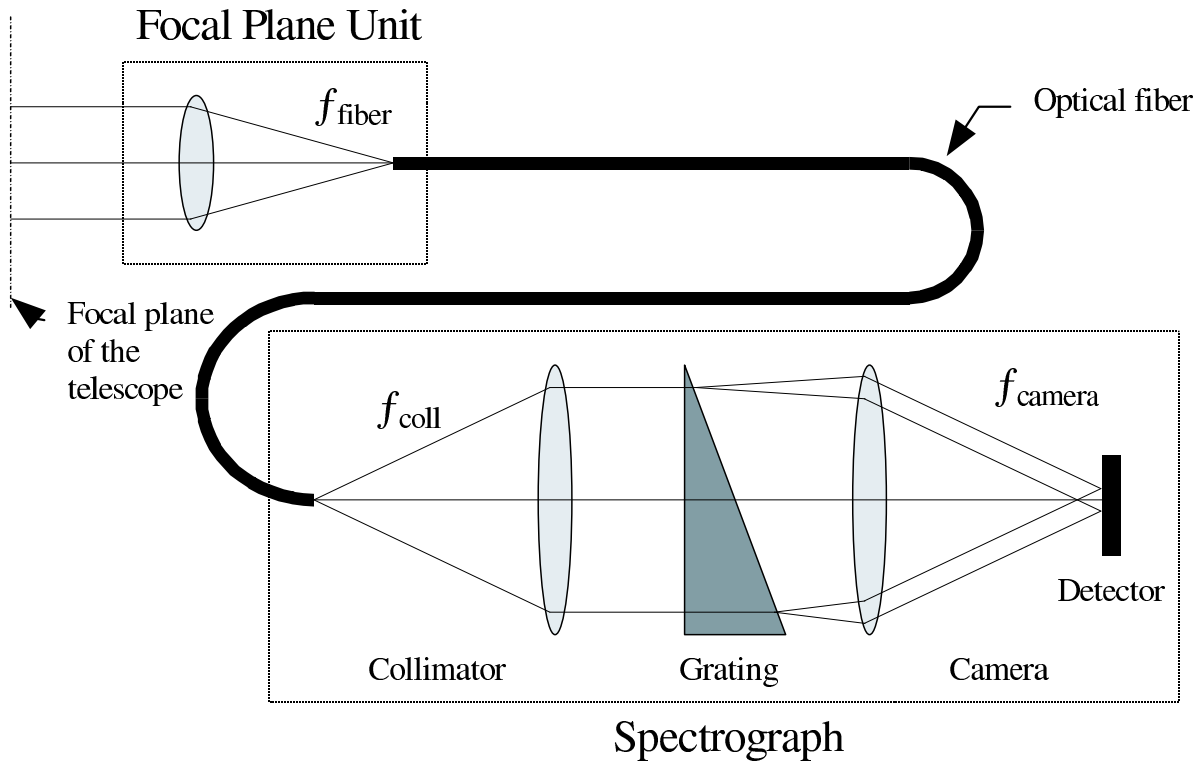


Fig. 2.— A spectrograph fed by an optical fiber. In this case, the focal plane unit images the telescope pupil onto the core of the fiber.

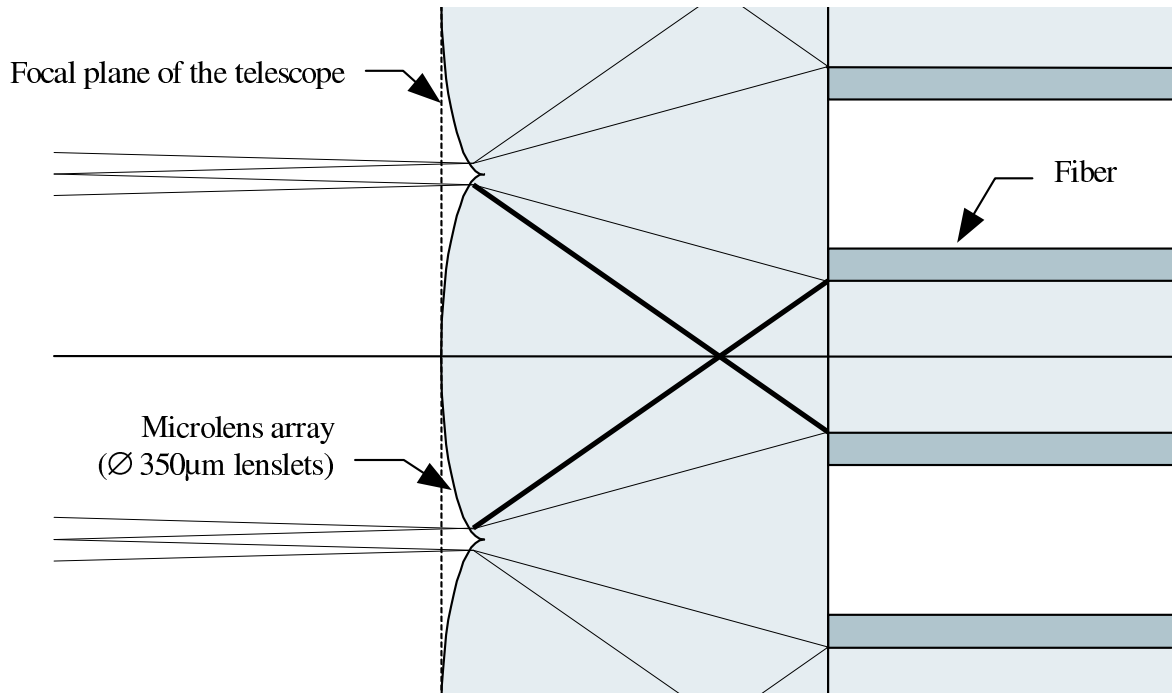


Fig. 3.— A microlens array feeding optical fibers. The thicker rays from the middle lenslet show how the edge of the fiber is fed with faster rays than those in the middle of the fiber.

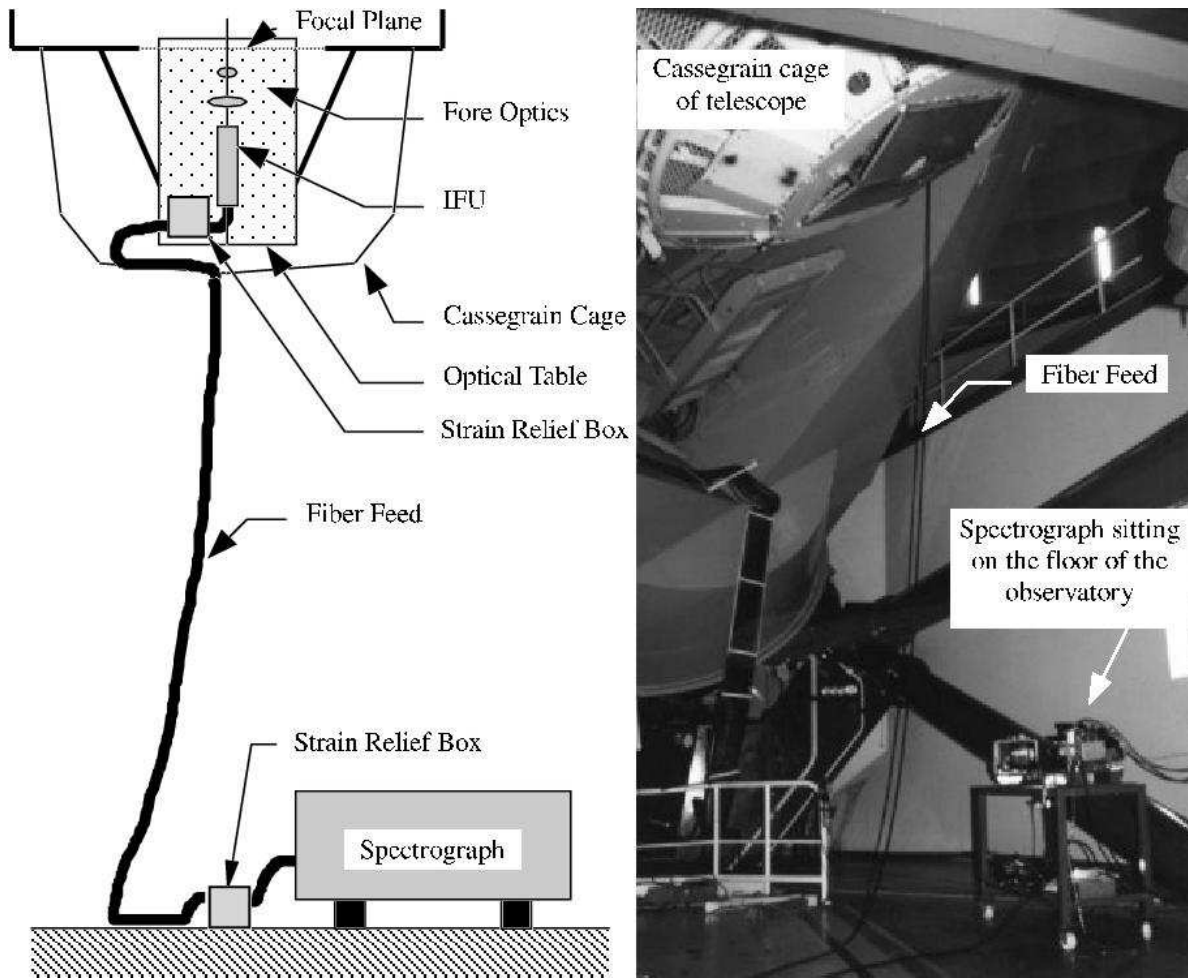


Fig. 4.— Layout of SPIRAL Phase A on the Anglo-Australian Telescope. The spectrograph is shown with its light-proof covers removed. The strain relief box for the fiber slit end is mounted underneath the spectrograph framework.

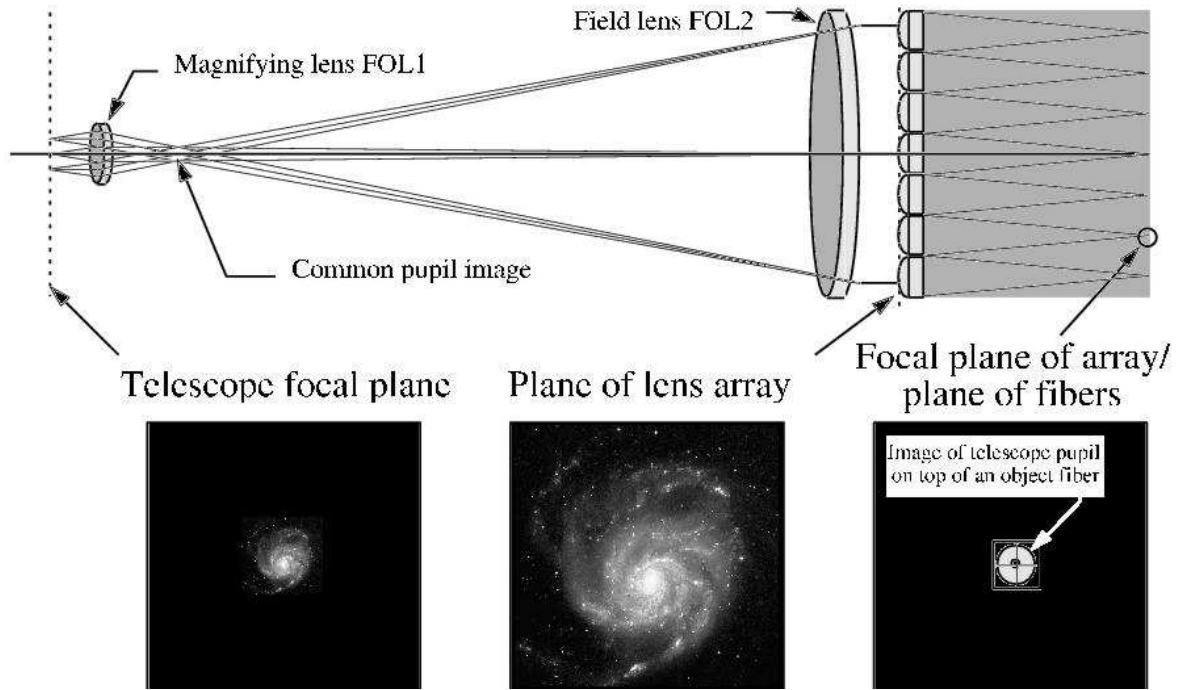
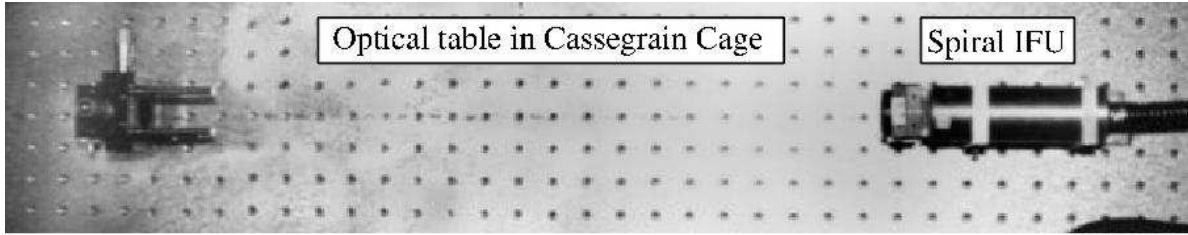


Fig. 5.— The fore-optics for the integral field mode. These two lenses act to magnify an extended object (such as a galaxy) to match the plate scale of the lens array with the seeing at the telescope. At the focal plane of the fibers each lenslet projects an image of the pupil onto the end of the object fiber.

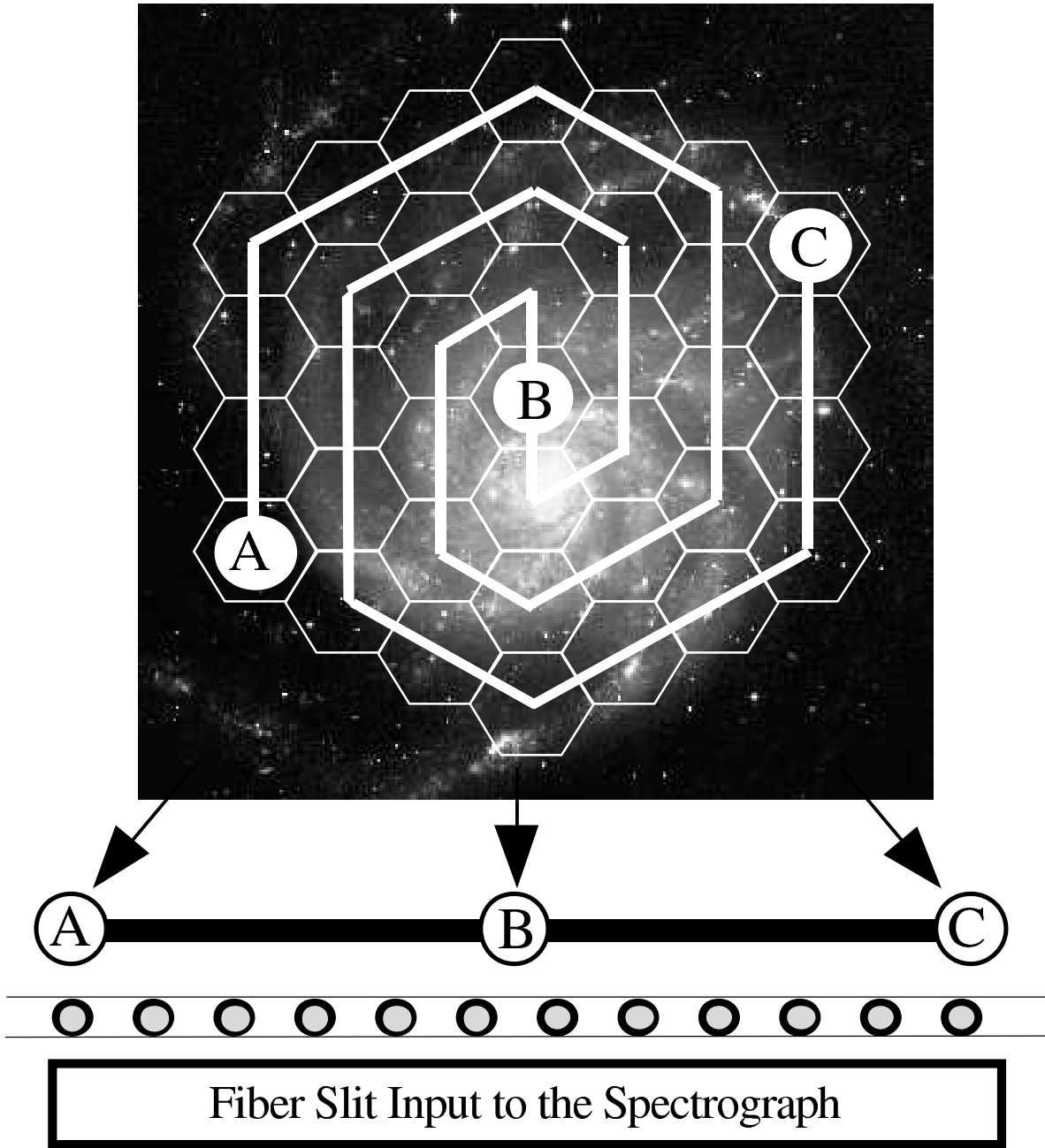


Fig. 6.— Schematic layout of the SPIRAL fiber slit. The fibers are reformatted from a spiral pattern on the sky into a long slit suitable for dispersion in a spectrograph. The spiral pattern ensures that fibers adjacent on the slit are adjacent on the sky.

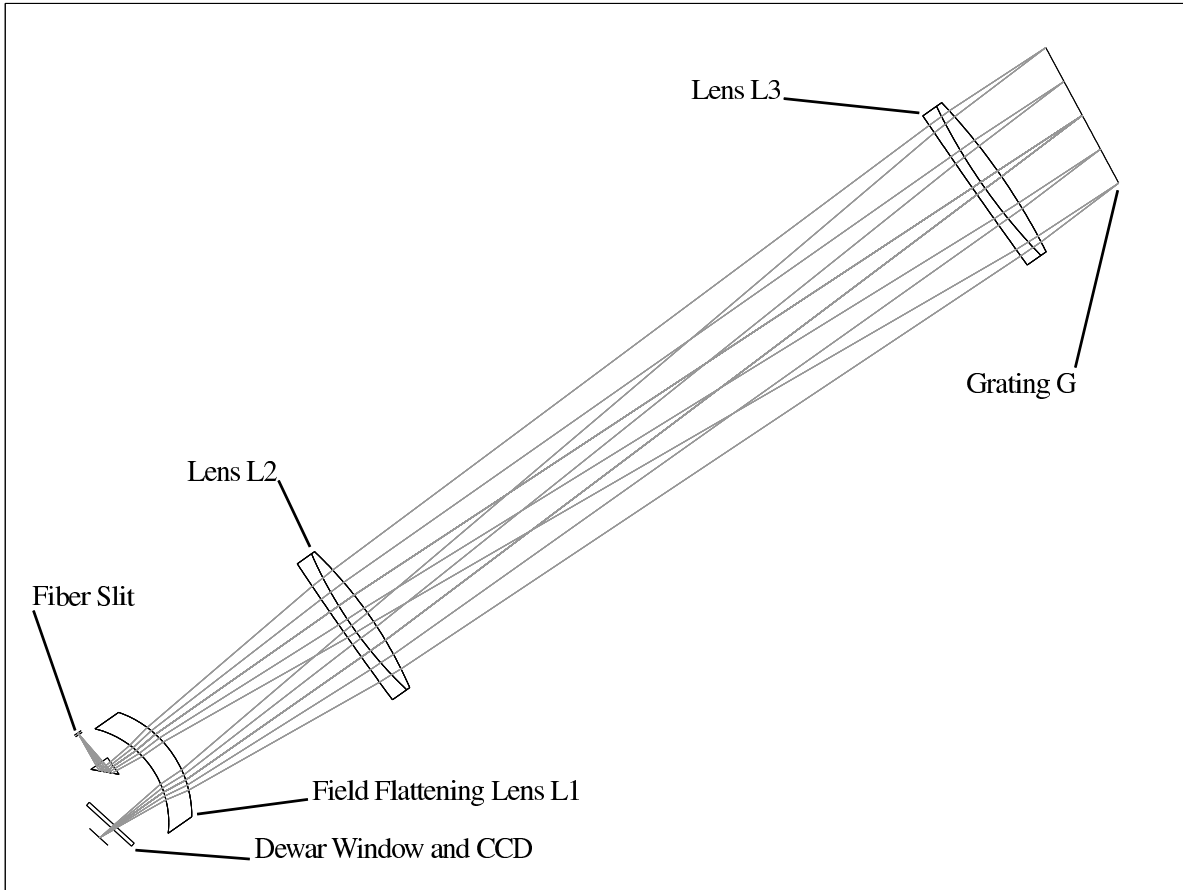


Fig. 7.— Optical layout of the SPIRAL spectrograph. Monochromatic light emerges from the fiber slit in this ray-trace and is folded by a prism into the Petzval system (L1,2,3). After being diffracted by the grating G1 the light passes back through the system and is focused on the detector inside the dewar (not shown).

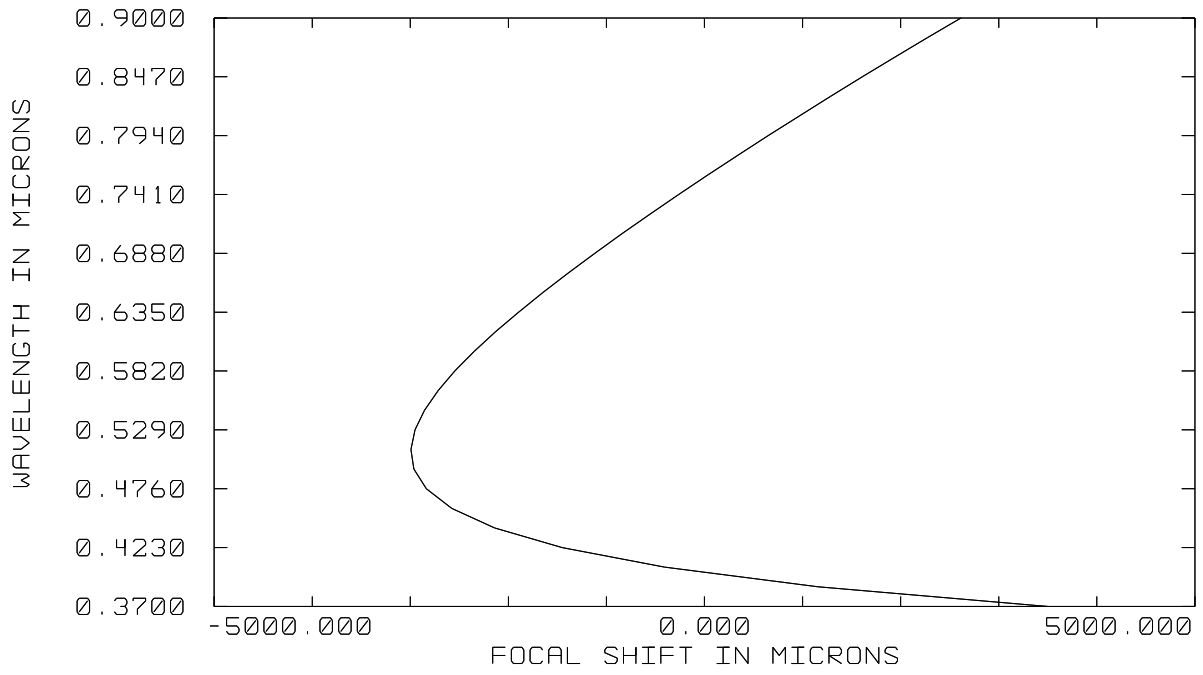


Fig. 8.— Chromatic focal shift for the SPIRAL spectrograph.

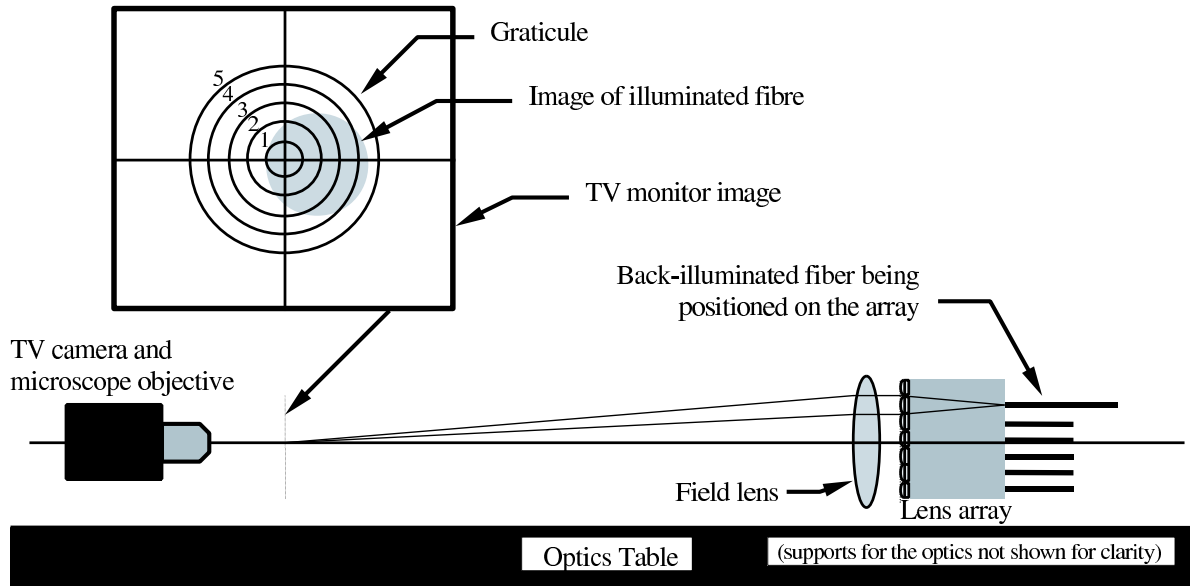


Fig. 9.— Optics used in the alignment of fiber ferrules on the back of the lenslet array.

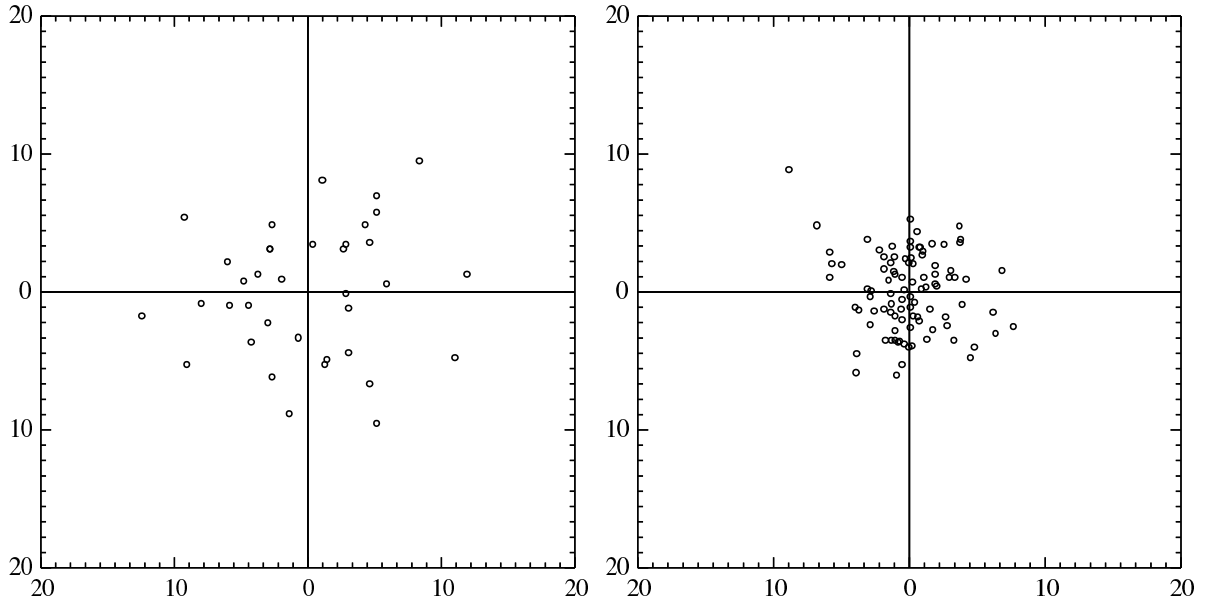


Fig. 10.— SPIRAL Phase A (left) and COHSI (right) decentering errors. Both plots have scales measured in microns centered on the mean fiber position.

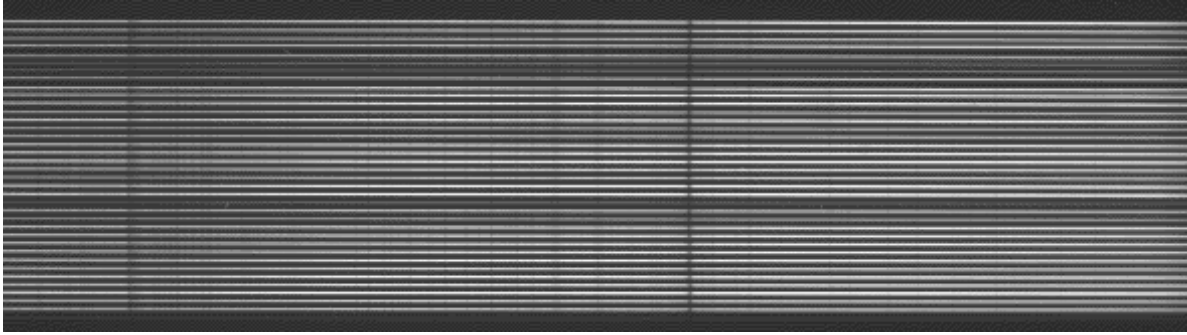


Fig. 11.— A raw IFS data frame. In this frame the dispersion axis is across the page and the 37 separate fiber tracks can be seen. This is a twilight sky exposure, clearly showing absorption features in the atmosphere and the variation in throughput between fibers.

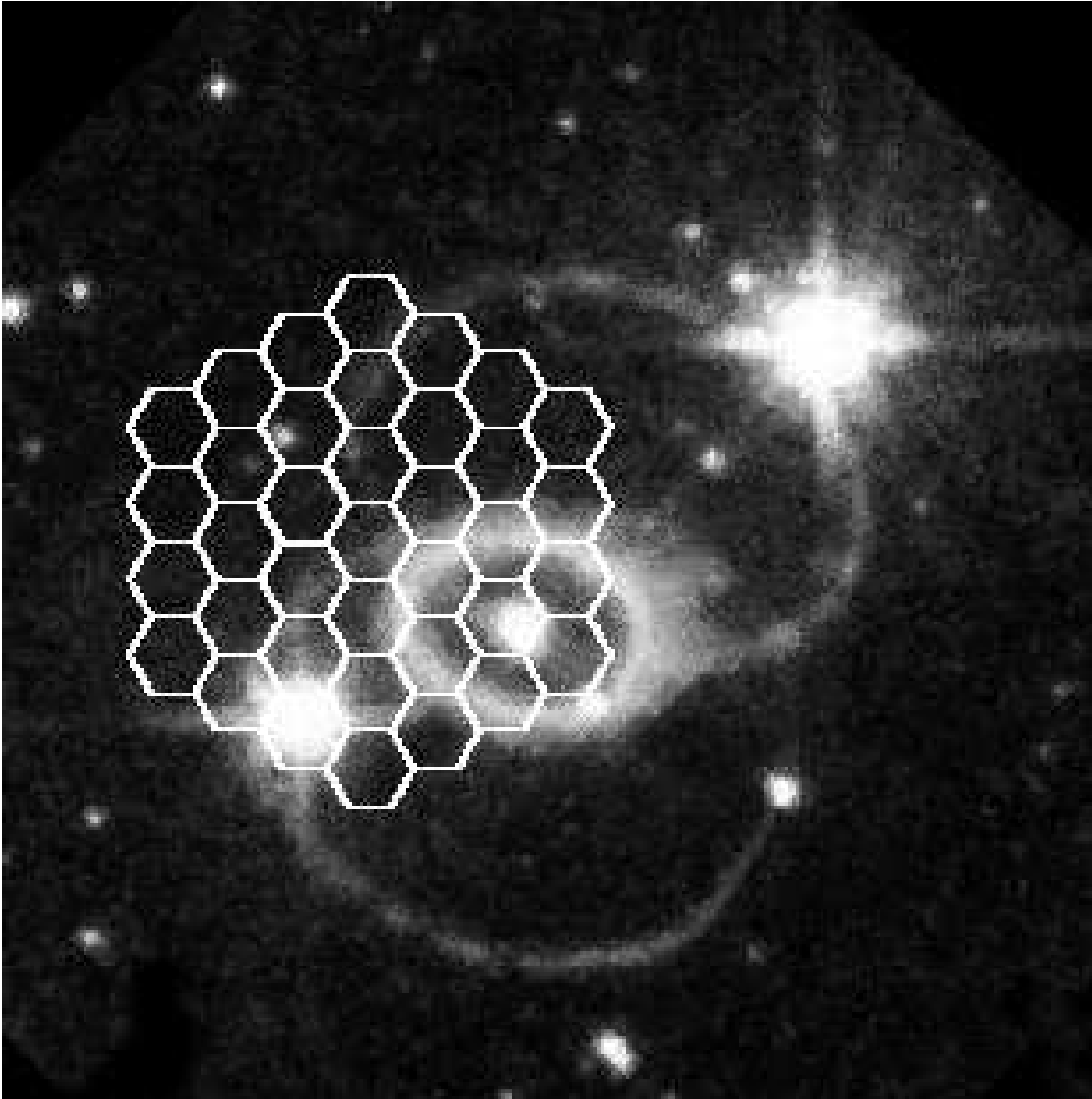


Fig. 12.— HST WFPC image of 1987A. The estimated position of the SPIRAL lens array is shown superimposed on the image. North is to the top and East to the left. (Photo: Chun Shing Jason Pun (NASA/GSFC), Robert P. Kirshner, taken on March 5 1995 in N II λ 6584).

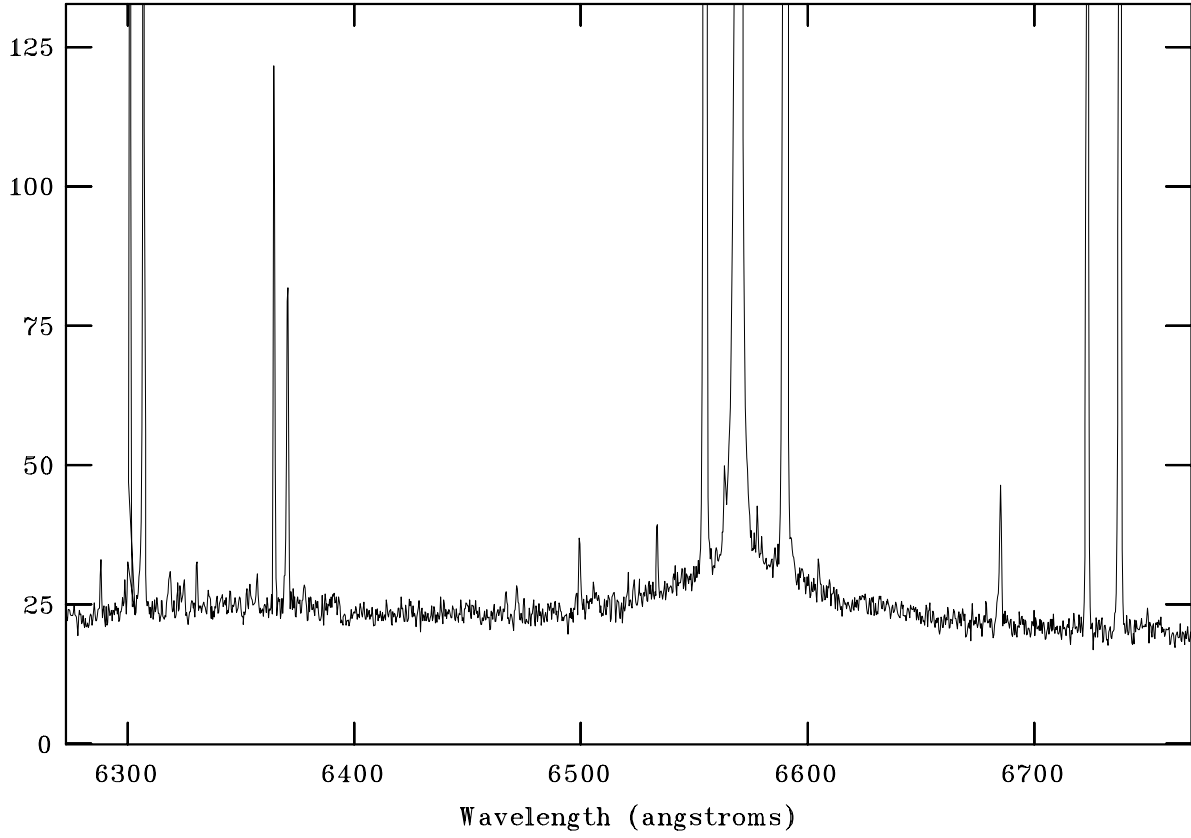
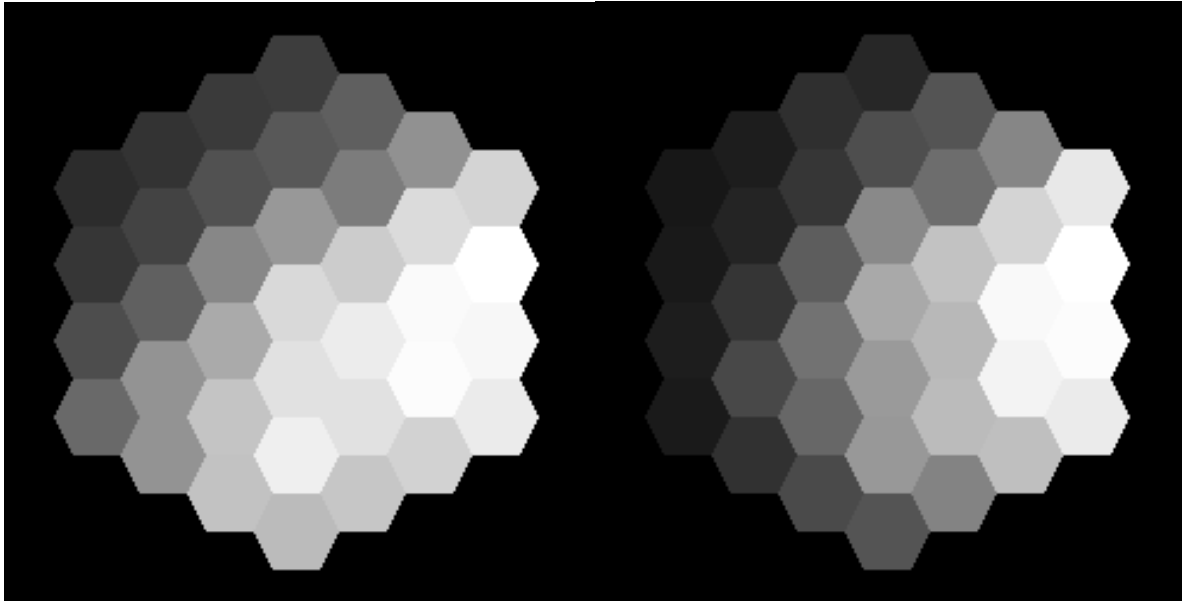
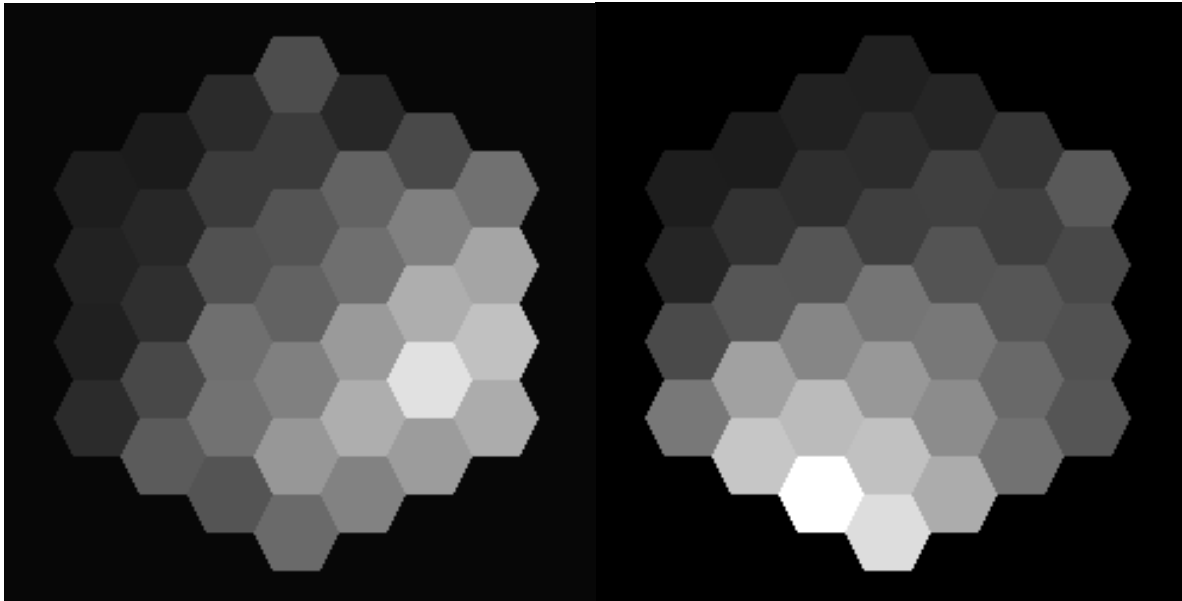


Fig. 13.— The SN 1987A spectrum. Superimposed on the bright narrow hydrogen line is a broad line contribution from fast moving ejecta.



HST F656 filter

[NII] λ 6583



Broad H α emission from SNe

Continuum $\lambda\lambda$ 6600-6800

Fig. 14.— SPIRAL maps of SN 1987A. All map intensities are normalised. North is top and East is left.

NOAO/IRAF V2.11EXPORT mak@cass00 Thu 12:21:24 12-Nov-98
[bd2_final]: INDEF ap:1 beam:1

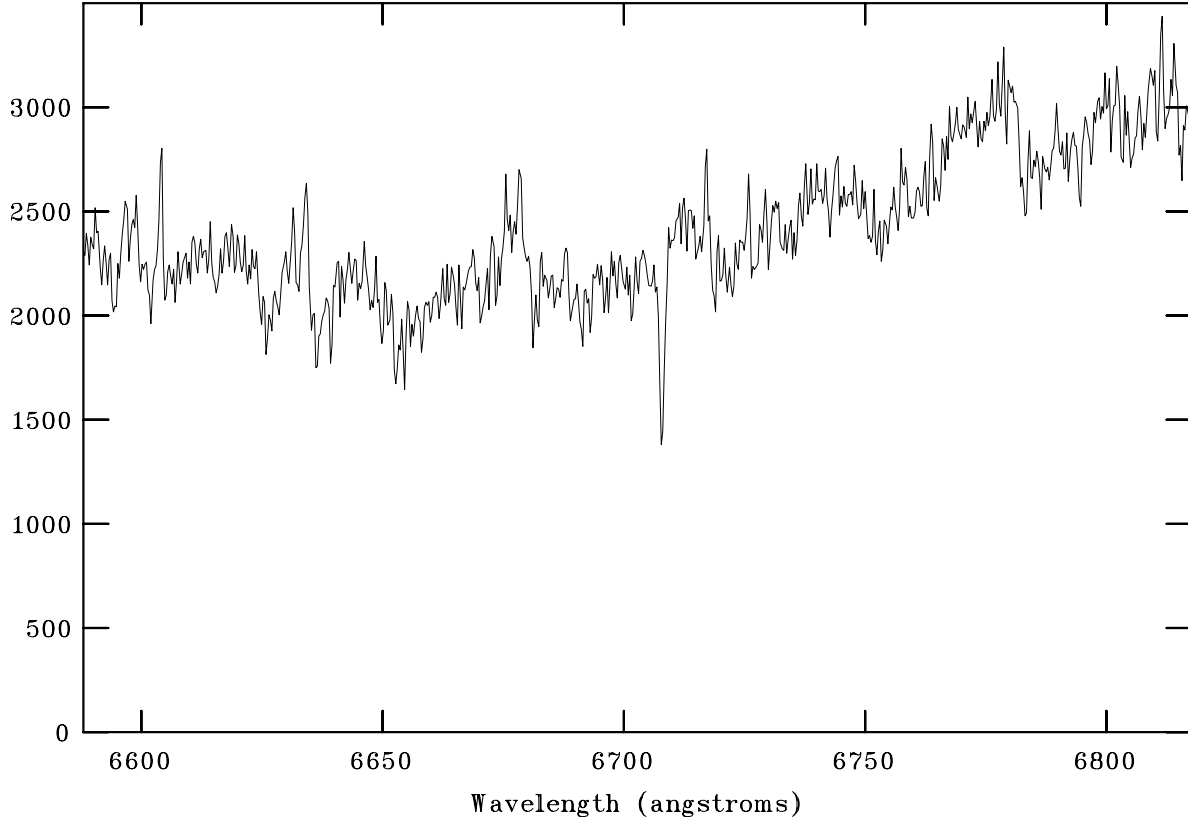


Fig. 15.— Spectrum of LP 944-20. The Lithium absorption line can be seen clearly in the middle of the spectrum. Flux is in arbitrary units.